J Mater Sci (2017) 52:613–627

Densification behaviour and microstructural evolution of Ti-48Al consolidated by spark plasma sintering

Hung-Wei Liu[1], D. Paul Bishop[1], and Kevin P. Plucknett[1,*]

[1] *Materials Engineering, Department of Process Engineering and Applied Science, Dalhousie University, 1360 Barrington St., Halifax, NS, Canada*

Received: 8 July 2016
Accepted: 31 August 2016
Published online: 7 September 2016

ABSTRACT

Spark plasma sintering (SPS) is a fairly novel powder metallurgy (PM)-based process. Compared with more traditional PM processes, SPS technology provides greater sintering efficiency for the Ti-48Al alloy, due to its fast heating and cooling rates, combined with an applied pressure and electric field during the process. In this study, three fundamental processing parameters (i.e. sintering temperature, time and particle size) are investigated, and their effects on densification, hardness and phase transformations are studied. Three grain morphologies were found in the microstructures, present in different ratios in the samples, depending on the sintering parameters. A model is proposed to explain the (α_2) grain-phase growth and the transformation of two types (fine and coarse) of lamellar structural development. The pore configurations (i.e. size and quantity) are examined, and their interactions with the phases, which suggest the phase-formation sequence and sintering state, are also discussed.

Introduction

Titanium aluminide (γ-TiAl)-based alloys have attracted considerable interest from the aerospace and, more recently, automobile industries, due to their low-density, and high retained strength and oxidation-resistance properties at elevated temperatures (>500 °C) [1]. These properties make TiAl an excellent material to replace the much heavier Ni-based superalloys for engine applications [2]. Several TiAl alloys have been developed in the recent decades, such as the Ti-48Al-2Cr-2Nb (GE) alloys, developed for low-pressure turbine applications [3, 4] and the Ti-43Al-4Nb (TNM) alloys for sheet components [5–8]. However, TiAl alloys generally suffer from low ductility particularly at room temperature, and thus they are difficult to manufacture when using more conventional thermomechanical processes. Consequently, the production cost is high, and the applications of TiAl alloys are greatly restricted. Many near-net shape approaches, which can considerably minimise the need for post-machining, have been investigated to overcome the poor workability of the material [9–11]. Among them, powder metallurgy (PM)-based processes can provide a cost-effective route, and do not possess the common concerns relating to compositional segregation during the casting process [12].

Address correspondence to E-mail: kevin.plucknett@dal.ca

DOI 10.1007/s10853-016-0358-x

One PM approach that has shown great potential in recent years is the spark plasma sintering (SPS) process [13–16]. This novel technology utilises a pulsing on–off DC current, and applies pressure to the powder simultaneously. In the case of conductive powders, the electrical current flows through the material, and heat is generated due to the Joule effect [17, 18]. The heating occurs between the particle contact regions, where the electrical resistance is the greatest. As a result, the SPS technique provides considerably localised and thus very efficient heating for metallic powders. Furthermore, because of the nature of the applied current, the SPS process also heats and cools very rapidly, and hence, grain growth can be significantly reduced. Very fine-sintered microstructures, with grain sizes from a few microns down to hundreds of nanometres, can be retained when using nano-scaled starting powders [19]. It is consequently possible to achieve comparable sintering results to more conventional methods, while using lower sintering temperatures and shorter holding times. For TiAl-based alloys, the sintering temperature is generally in the range of 1100–1300 °C range, which is held for less than 10 min in a SPS process. In comparison, the conventional hot-pressing method typically requires a hold time of 1–2 h at temperatures of 1300 °C or even greater, [3, 20]. Besides the thermal effects, it has also been demonstrated that the electrical field generated from the current also imposes pronounced influences on mass transportation during sintering. Munir and colleagues have published a detailed review discussing the field effects in the SPS process, which are related to these phenomena [21].

In early TiAl PM research, using the pressureless press-and-sinter method, several works have demonstrated significant swelling in the samples when sintering elemental Ti and Al blends. Although some SPS investigations were conducted using the more economical blended elemental route successfully (with Ti and Al elemental mixtures), Kirkendall porosity and compositional inhomogeneity were still prevalent [22, 23]. Moreover, further studies using SPS or hot-pressing approaches have reported that the Al melt can be squeezed out of the powder mixture when sintering elemental Ti and Al blends [3, 24]. Therefore, in the present study, a pre-alloyed TiAl powder was initially produced in-house for the SPS assessment. The pre-alloyed TiAl powder was produced by pressureless heat treatment of a blend of elemental Ti and Al, and the partially sintered porous products were crushed and milled to a refined particle size and then used as the precursor powder for the SPS investigation.

The present study reports on the fundamental sintering responses of a γ-TiAl/α_2–Ti_3Al alloy powder using the SPS approach. The effects of processing parameters (i.e. temperature, time, particle size) on the sample densification were studied, and the sintered microstructures were analysed, with an emphasis placed on the phase formation and evolution, and the relationship of porosity with other phases in the materials.

Materials and methodology

The pre-alloyed Ti-48Al (all compositions are given as atomic percentage, unless stated otherwise) powder was prepared in-house using elemental raw powders, specifically a sponge titanium powder (−100/+325 mesh; ADMA Products Group, Hudson, OH, USA), and an aluminium powder (Grade DG20; Ecka Granules, Fürth, Germany). The elemental blend was initially pressed into discs, and subsequently heat treated at 1200 °C for 2 h in a tube furnace (Model STT-1600C, SentroTech, Stronsville, OH, USA) under constant argon flow. The heating and cooling rate were controlled at 5 °C min^{-1}. The cooling rate decreased to a natural furnace cool when the temperature dropped below ~200 °C. The heat-treated discs were then roughly crushed using a manual press. Further grinding was conducted within a 250-ml alumina bowl on a shatterbox mill (Model TM/MAX2, TM Engineering Ltd., Burnaby, BC, Canada) operating at 950 rpm, for a duration ranging between 90 and 600 s. The particle size distributions were measured using a particle size analyser (Model Master Particle Sizer 20600, Malvern Instruments, Malvern, UK).

Once the powder was prepared, a ~6-g batch was loaded into a graphite die set, which consisted a 20-mm-diameter die with upper and lower punches. Graphite foil was used to cover the die interior and the punch surfaces prior to powder loading to minimise potential reaction with the die set itself. The die set was subsequently loaded into the SPS system (Model SPS Model 10 Series, Thermal Technology LLC, Santa Rosa, CA, USA) to consolidate the powders. To ensure no residual air in the chamber, the

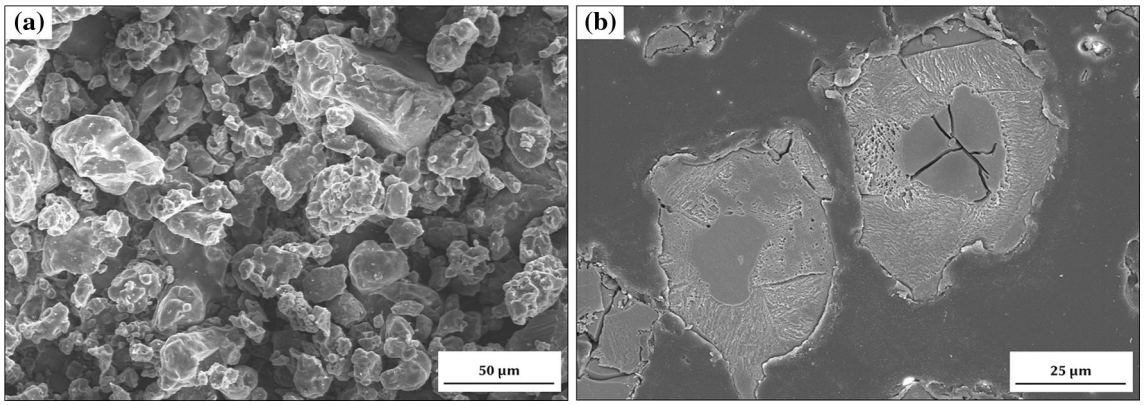

Figure 1 Morphology of **a** the 'in-house' manufactured Ti-48Al pre-alloyed powder after hand grinding (combined SE/BSE image), and **b** the polished and etched cross-section of the powder (low negative bias BSE image).

SPS furnace was evacuated and back-filled with argon twice. When the vacuum was found suitable ($<2 \times 10^{-2}$ torr), the sintering process was performed at temperatures ranging from 800 to 1300 °C, with an isothermal hold time ranging from 0 to 10 min. A pressure of 50 MPa was applied to the sample during the heating process. The current and voltage of the SPS process were automatically controlled by the system computer to follow the heating scheme. The heating and cooling rates were controlled at ~100 °C min^{-1}. A pyrometer was used to monitor the temperature (effective at above 600 °C). After the samples had cooled, the graphite foil was removed by light sanding to reveal the surface of the SPS-processed samples.

The sintered density was subsequently determined using the oil immersion method, in accordance with ASTM Standard B328 (MPIF Standard 42). The specimens were then polished for microstructural analysis. Kroll's solution (2 ml HF, 6 ml HNO_3, 92 ml H_2O) was used to etch the selected samples. The crystalline phases of the SPS-densified samples were identified using X-ray diffraction (XRD; Model D8 Advance, Bruker Instruments, Madison, WI, USA). The microstructures were examined using an optical microscope (Model DP-71, Olympus Corp., Tokyo, Japan), with differential interference contrast (DIC) imaging, or a scanning electronic microscope (SEM; Model S-4700, Hitachi High Technologies, Tokyo, Japan). The SEM was operated in either combined secondary electron (SE)/backscattered electron (BSE) mode, or with a negative bias to limit the imaging mode to BSE. Local compositions of phases were determined using an energy-dispersive X-ray spectroscopy (EDS; Model Inca X-MaxN, Oxford Instruments, Concord, MA, USA) in the SEM or a wavelength-dispersive X-ray spectroscopy (WDS) in an electron-probe micro-analysis system (EPMA; Model JXA-8200 Superprobe, JEOL, Tokyo, Japan). Carbon content was measured using a carbon/sulphur analyser (Model Eltra CS-2000, Eltra GmbH, Haan, Germany). The pore size (Feret diameter) and the area fraction statistics were measured and compiled using optical images and the analysis software ImagePro 6.3 Plus (MediaCybernetics, Rockville, MD, USA). Each dataset was composed of more than 500 measurements. The hardness characteristics of the sintered samples were measured using a Rockwell hardness tester using the HRA scale (Model Wilson® Rockwell 2000, Buehler Corporation, Lake Bluff, IL, USA).

Results and discussion

Material characterisation

The basic morphology of the fabricated Ti-48Al powder, after hand grinding, is shown in Fig. 1a. Cross-sectional examination of the powder revealed an internal 'core–rim' structure (Fig. 1b). EDS analysis indicated that the core region contained a higher Ti concentration (~61 %), while the surrounding rim area has lower Ti (~51 %). The powder structure was formed as a result of elemental Ti and Al sintering. When the powder is milled using the shatterbox, this complex internal structure was broken down through attrition, and the two phases were then expected to be well distributed in the resulting powder blend. The particle size distribution achieved after various

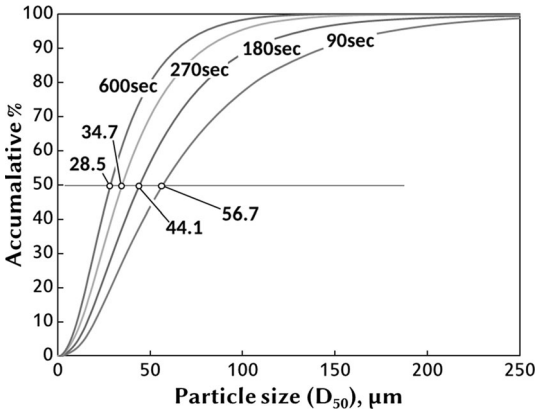

Figure 2 The measured particle sizes (D_{50}) of the Ti-48Al powder after various grinding times.

milling times, in terms of the relative D_{50} value, is shown in Fig. 2.

Densification, hardness and carbon contamination

In this set of experiments, the SPS process was only conducted using a 3-min isothermal hold, and consequently the effects of temperature were specifically explored. Figure 3 demonstrates that, as might be anticipated, the powder densification response is strongly temperature dependent. Despite the short sintering time, almost fully dense material can be achieved with a 3-min hold at 1300 °C (98.9 % of theoretical density), showing excellent efficiency for the SPS process. In contrast, from our earlier work, samples conventionally vacuum sintered using a tube furnace only attained ~88 % of theoretical density when using a 4-h hold at 1300 °C. In this respect, the advantage of the SPS process is clear against more conventional sintering. Nevertheless, in a SPS study using a pre-alloyed (i.e. Ti-47Al) powder, full densification was achieved at noticeably lower temperatures (at as low as 1000 °C) than the present work [25]. The improved densification was potentially due to higher kinetics during sintering when using the mechanically alloyed powder [25]. The milled powder had complicated shapes with more inner pores and defects, and the differences in morphology may contribute to different densification mechanisms. Guyon et al. consolidated two TiAl-based powders (an atomised powder versus one that was milled) using SPS, and they observed that the milled powder experienced a different deformation mode (grain boundary sliding assisted by surface/grain boundary diffusion) during densification, while for the atomised powder, heterogeneous deformation modes promoted by dislocation glide and twinning occurred [15]. In another SPS work, comparing various types of Ti powder (gas atomised, hydride/de-hydride and sponge), the densification sequences were different for the respective powders, and their sintered microstructures were distinctly dissimilar, although sintering of the individual powders all resulted in full densification after the process [26]. However, it

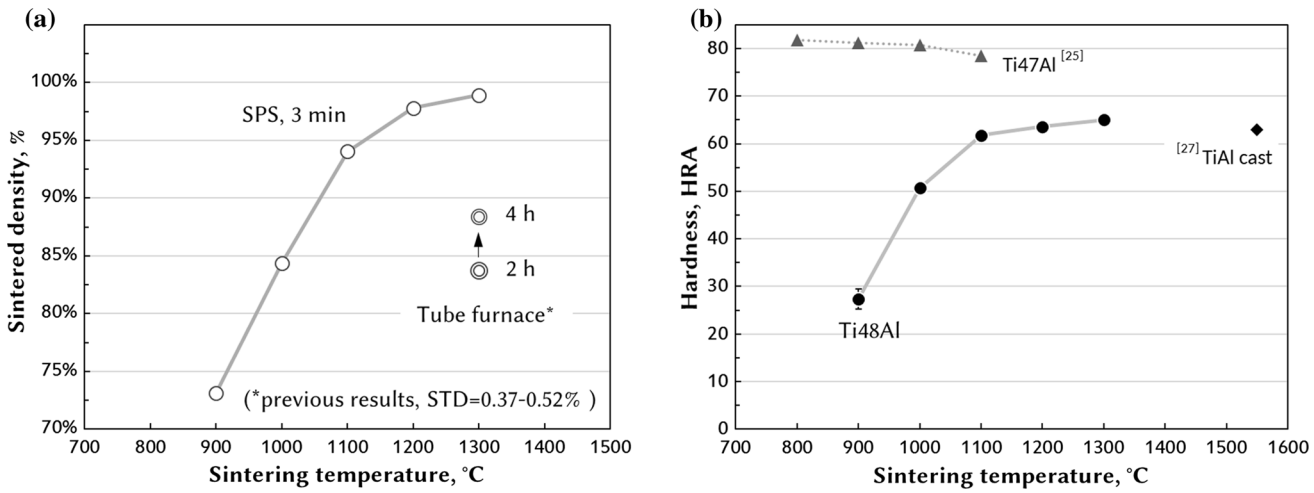

Figure 3 **a** The effects of SPS temperature on the density of the sintered samples, as a percentage of theoretical (standard deviation error = 0.18 % at 1200 °C). **b** The hardness of the sintered samples as a function of SPS-processing temperature. The reference data are acquired from Refs. [25, 27]. Note that the standard deviation errors for the Ti48Al samples were very small, and are only apparent for the porous 900 °C-processed sample.

should also be noted that the measured SPS-processing temperature is actually directly on the die in most SPS systems, and hence not the true reaction temperature of the sample itself. This temperature difference can vary substantially, depending on the material [17]. The use of a pyrometer in the current experiments might also cause some differences in temperature measurement compared with other experiments conducted when using a thermocouple. As a consequence, direct comparison between SPS experiments using different facilities can be difficult.

In the present study, full densification might be realised if the sintering temperature was raised above 1300 °C. However, sintering at 1300 °C unexpectedly caused an issue where part of the sample was bonded with the punch. It was speculated that some powder likely passed the graphite foil and became bonded with the contact surface of the punch. As a consequence, in order to continue the study, sintering temperatures higher than 1200 °C were not considered further, in order to avoid potential damage to the equipment.

Although the present study did not fully investigate the mechanical properties of the SPS-processed samples due to size limitations (20 mm diameter), their hardness properties were evaluated as a general indication. As illustrated in Fig. 3b, the hardness values of the sintered materials follow the general density trend. The values for the samples that are close to fully dense (i.e. those sintered at 1200 and 1300 °C) are comparable to the values reported for a nominal TiAl cast material (despite the fact that the two-phase Ti-48Al is harder, due to the presence of Ti_3Al phase) [27]. When compared with a broadly similar composition (Ti-47Al) in another SPS study, those hardness values are higher than the present ones even at lower sintering temperatures, due to their higher sintered densities (their materials were nominally fully dense) [25].

Another important factor in a sintering process is the isothermal heating time. In the present study, a series of sintering experiments, using various hold times, were conducted with the sintering temperature maintained at 1200 °C. Figure 4 illustrates the effects of sintering time on sample densification. It is clearly seen that although the density initially improves with time, there is no further improvement after 5-min hold. In comparison, Fig. 4 demonstrates that the hardness decreases with increased hold time. This observation can be ascribed to grain growth after the

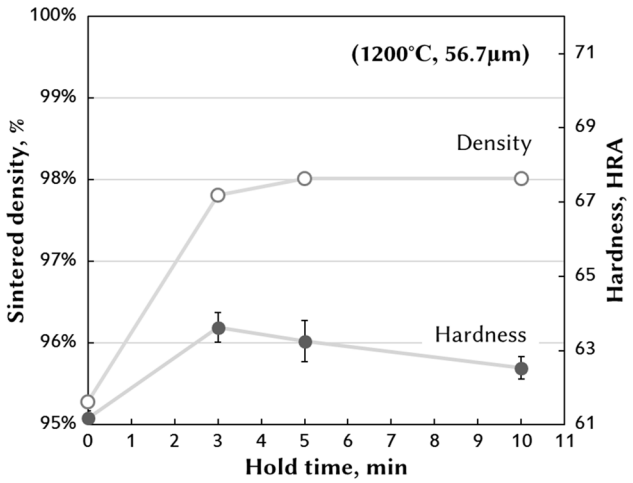

Figure 4 The effects of SPS hold time on the density, as a percentage of theoretical (standard deviation = 0.18 % at 1200 °C), and the hardness of the sintered samples as a function of SPS-processing hold time.

longer sintering times. Further details regarding the grain growth response will be discussed in the subsequent section. The current results suggest that a 3–5-min hold is adequate, while a longer sintering time could be detrimental to the mechanical properties. As mentioned in the Introduction, the SPS process is generally conducted with a hold period of less than 10 min, and near fully dense TiAl-based alloys can be produced in this manner. Any excessive sintering time would promote unnecessary grain growth and impair the mechanical properties.

As the sintering process is conducted in a graphite die, carbon contamination was anticipated, even though the sintering process was considerably shorter in duration compared with other traditional, slower heating techniques (e.g. electric heating furnace). This is a common concern in any SPS process using a graphite die and punches. Table 1 lists the carbon concentration from the raw powders to the final SPS-densified products. The carbon concentration was considerably increased when prolonging the sintering residence time in the SPS die. Formation of the titanium carbide (TiC) phase was identified by XRD analysis, although no clear titanium carbide phase was observed from SEM examination of the microstructure and associated EDS analysis. As shown in Fig. 5, the sintered materials generally exhibit an XRD pattern showing a mixture of the γ-TiAl–α_2-Ti_3Al phases, while two TiC peaks are also clearly distinguished. The formation and existence of the TiC might influence the mechanical properties of

Table 1 Carbon concentrations at different processing stages

	ppm
Elemental Ti/Al blend (raw)	53[a]
Pre-alloyed TiAl	65[a]
Shatterbox milled (90 s)	74[a]
Spark plasma sintered (1200 °C/3 min)	183
Spark plasma sintered (1200 °C/10 min)	675

[a] Measurement is close to the detection limit

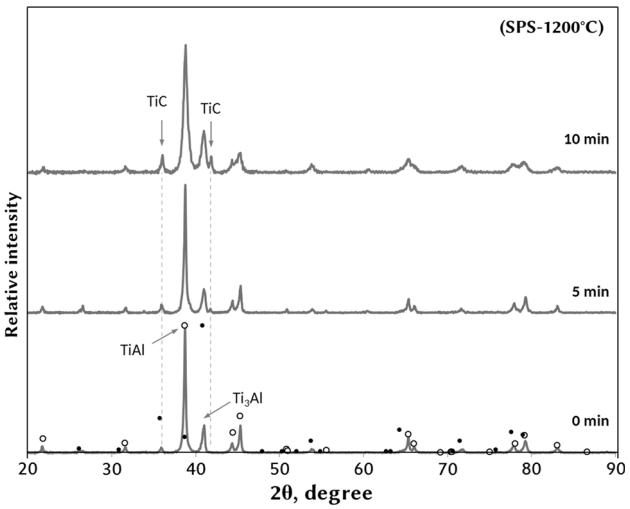

Figure 5 XRD patterns obtained for the Ti-48Al powders after different SPS hold times, showing increasing TiC formation with longer sintering time (1200 °C sintered samples).

the TiAl alloy, but its effect is beyond the scope of the present study.

The present work also investigated the effects of Ti-48Al particle size on the SPS process. In solid-state sintering, a smaller particle size translates to shorter distances for diffusion, and a greater number of contacting points for bonding between particles. The present synthesised Ti-48Al powder was ground down to several different ultimate particle sizes in the shatter box mill, as previously outlined in Fig. 2. As expected, a decreasing initial particle size resulted in better densification during sintering (Fig. 6). Furthermore, use of the finer powder resulted in an earlier shrinkage onset, and the difference continued to increase until the peak temperature was reached, as demonstrated by the SPS ram displacement curves (Fig. 6b). The two shrinkage curves for the same coarse powder closely overlap, indicating consistent measurements. Improved densification using the fine powder is likely to arise, at least in part, from a higher concentration of particle–particle contact points during the SPS process. The sample hardness also increased accordingly, as the sintered density was improved. However, longer grinding time would give rise to higher contamination from the grinding environment. There are significant measured increases in oxygen and nitrogen concentrations from the atmosphere when conducting extended grinding for 30 min (data not shown). Although the grinding time was much shorter for the samples presented in the present work, contamination should always be minimised as much as possible. The outlined contaminating elements can be expected to be interstitially located in the alloy, and will most likely alter the mechanical properties.

Microstructural analysis

Phase identification

Detailed microstructural analysis of the samples sintered at temperatures below 1300 °C generally identified four phase categories following etching, as presented in Fig. 7. The samples sintered specifically at 1300 °C will be discussed in the next section as the microstructures are greatly dissimilar, due to a rapid diffusion mechanism. In Fig. 7, the rounded grain includes a smooth surfaced core (region A), and a surrounding region (B) which exhibits a light impression of parallel lamellar lines. Some grains can contain the lamellar lines internally (Fig. 7a), while other grains may only possess entirely A- or B-type features. Further away from this grain in Fig. 7a is a 'roughened' area with several morphologies (identified as regions C1–3 and D). While the regions C1, C2 and C3 appeared to exhibit very dissimilar appearances, they exhibited very similar compositions. The morphological differences were therefore likely due to different crystalline orientations and the way these differing orientations responded to the etchant. On the other hand, area D appeared less rough in terms of the surface texture. The four categories were not only determined by the appearance, but also grouped based on their compositions. Figure 8 schematically illustrates the composition range for each of the groups on the Ti-Al phase diagram, based on both the EDS and WDS results. The four features were distinguished as follows: (1) A—α_2 grain, (2) B and C—α_2/γ two-phase area and (3) D—γ-phase. It was clear that the Ti concentration decreased moving away

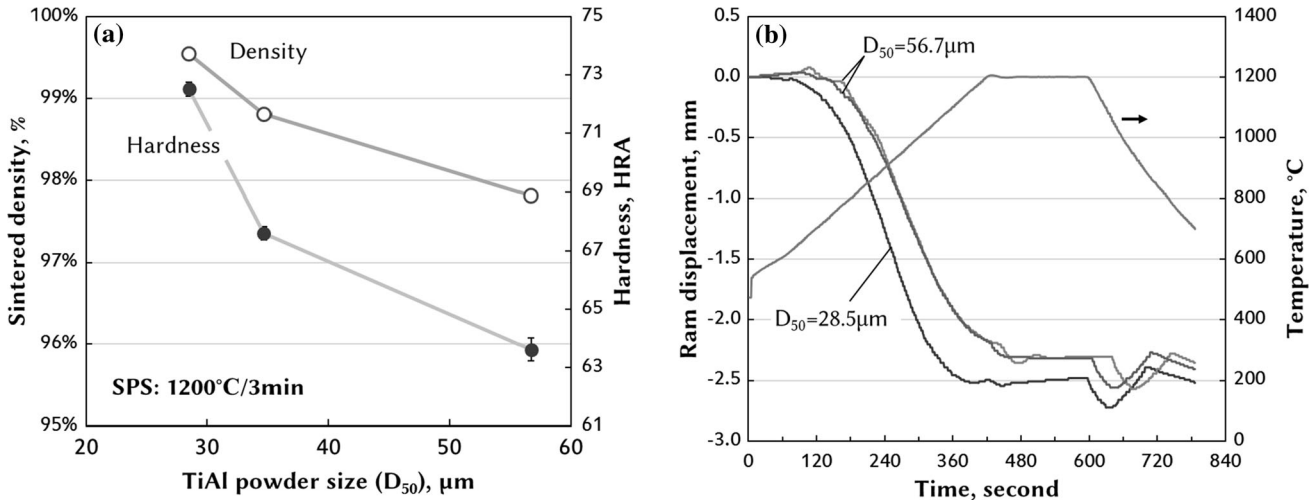

Figure 6 **a** The effects of Ti-48Al particle size on the sintered density (1200 °C/3 min) and HRA hardness. **b** SPS densification curves (i.e. ram displacement) for the fine (D_{50} = 28.5 μm) and coarse (D_{50} = 56.7 μm) Ti-48Al powders through the sintering process; the reproducibility of the process is highlighted from the duplicate curves obtained with two coarse powder samples.

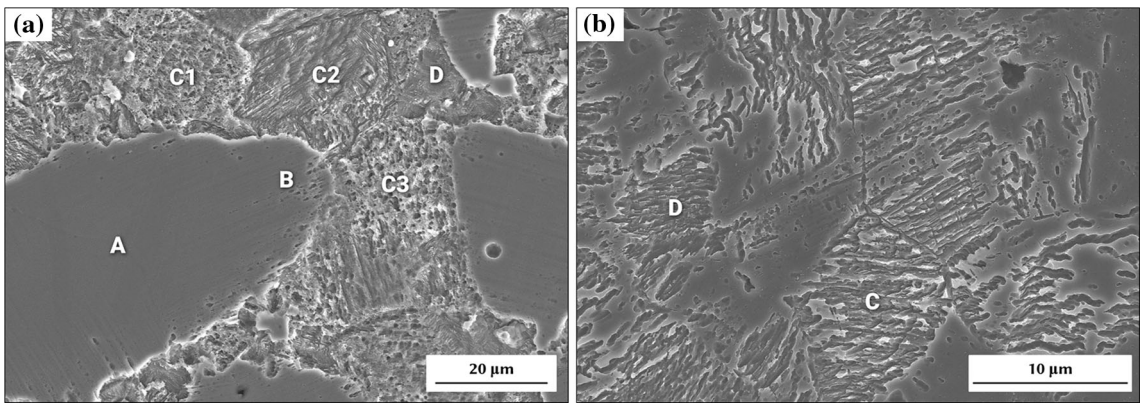

Figure 7 **a** SEM image highlighting typical phase features in a sample sintered at 1200 °C/5 min (combined SE/BSE image). **b** SEM image showing typical microstructural features for a lightly etched sample sintered at 1200 °C/3 min (combined SE/BSE image).

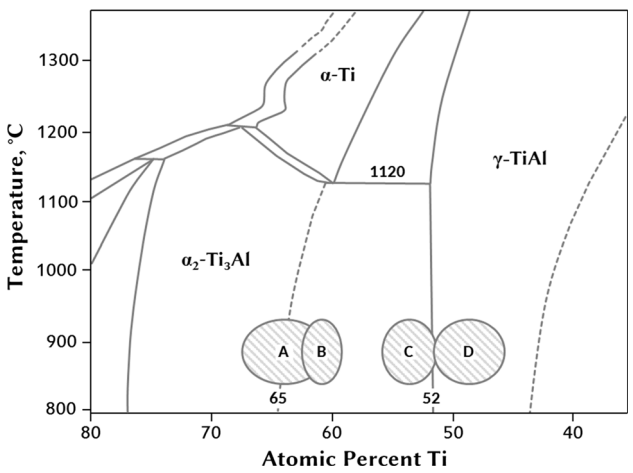

Figure 8 Schematic representation of the composition range for each identified microstructural feature; the section of the Ti-Al phase diagram is adapted from [28].

from the core to area B, and then region C, and it is the lowest in area D.

Although both regions B and C were in the two-phase range, they exhibit different morphologies due to differing γ:α_2 ratios. Area B contained more α_2-phase and had fine lamellar lines, whereas area C had more γ-phase and showed a rougher surface. It was difficult to characterise the rough surface from the etched micrographs. However, from the lightly etched SEM micrographs (Fig. 7b), a coarser lamellar structure is suggested within region C before it was severely etched. When comparing the lightly and regularly etched micrographs, the Ti-rich regions were more resistant to the etchant; those regions (i.e. A and B) appeared smooth in the SEM, or bright under the optical microscope. Those findings suggest the γ-phase exhibited a coarser lamellar structure and

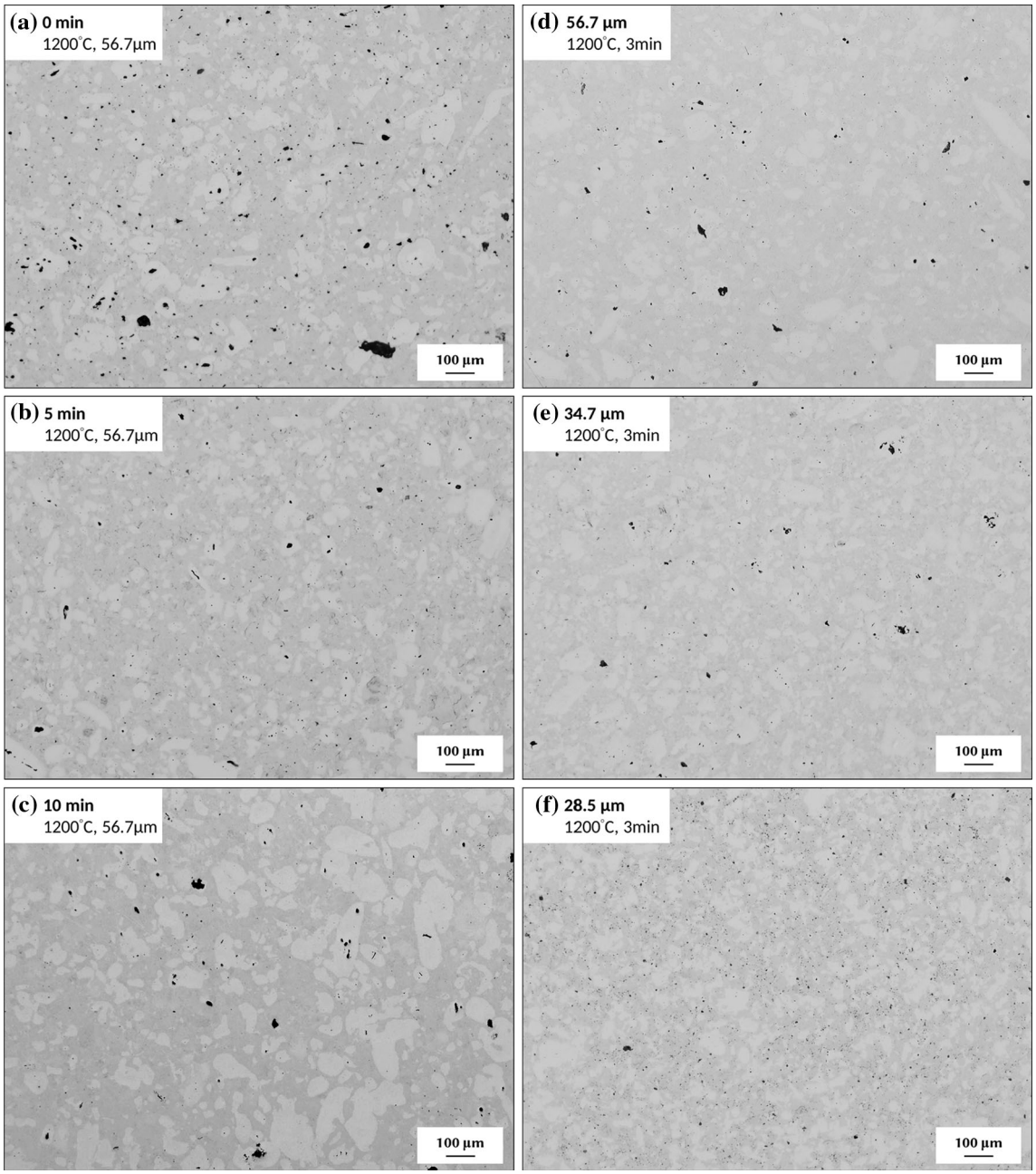

Figure 9 Representative optical micrographs of sintered samples processed using different sintering hold times, ranging from 0 to 10 min (**a**–**c**); and particle sizes ranging from 56.7 to 28.5 µm (**d**–**f**).

was more prone to etching (lower Ti content). The development and structure of the grains and the two-phase regions will be discussed in the following section.

α_2- and lamellae-phase development

As discussed previously, after processing at 1200 °C the SPS-processed material consisted of a combination of α_2 grains, the composite α_2/γ area, and the separate γ-phase. The two basic phases constitute the microstructures with different ratios and forms, depending on the processing parameters: sintering temperature, time, and initial particle size. To analyse the evolution of α_2 grains, polished and unetched optical micrographs were assessed. Although the grain size was not measured statistically, the growth and nucleation of grains were

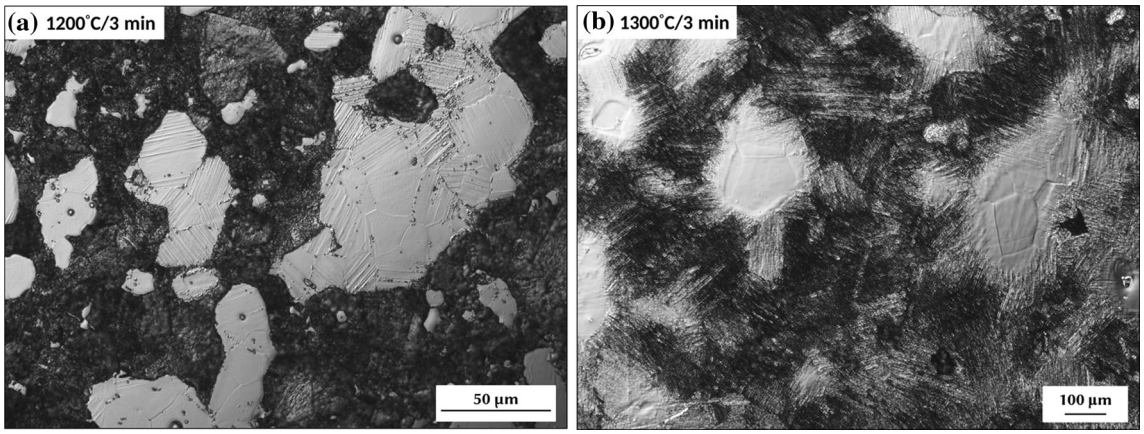

Figure 10 Representative DIC optical microscopy images of: **a** the internal microstructure in the α_2-Ti_3Al grains (SPS processed at 1200 °C/3 min), and **b** hexagonal core-structural formation when the sintering temperature was increased to 1300 °C (held for 3 min).

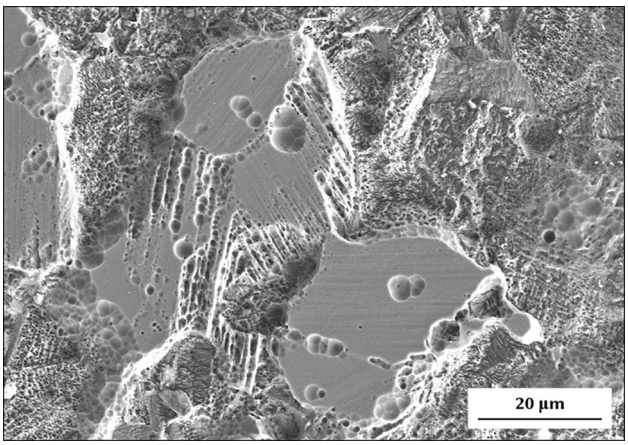

Figure 11 Typical SEM image showing initiation of the lamellar-structural formation after SPS processing at 1200 °C/5 min (combined SE/BSE image).

observed. In Fig. 9a–c, the grain size increases notably with the increasing sintering time. Such grain growth was also confirmed by the α_2 peak growth in the XRD analysis (Fig. 5). Furthermore, as discussed in "Densification, hardness and carbon contamination", the apparent stagnation of densification with longer sintering time also suggested the conditions for grain growth had been reached.

With reduced initial starting powder size, the resultant α_2 grains were smaller (but present in a comparable concentration) in the sintered microstructure (Fig. 9d–f). As noted earlier, the grain structure was, at some level, inherited from the powder. Consequently, when the particles were broken down further with longer milling time, more core (Ti-concentrated) fragments were exposed, which consequently developed into α_2 grains, dispersed uniformly in the sintered microstructure. When the starting powder was smaller, there was a higher concentration of particle–particle contact points, which could promote nucleation of the α_2 grains. If sufficient sintering time was provided, these newly nucleated grains might still grow. Nevertheless, the amount of α_2 grains was ultimately governed by the overall composition of the material. From the Ti-Al phase diagram, the α_2-phase is less than 7 vol.% of the Ti-48Al material (the remainder being the γ-phase) at room temperature. Besides the α_2-phase growth, more apparent grain growth was contributed from the α_2/γ (i.e. area B mentioned previously in "Phase identification") lamellae formation.

Assessing sintering temperature, the grains did not develop in size notably at the lower sintering temperatures, as there were still significant amounts of pores and densification was still predominant. Using optical DIC imaging, the internal structure within the grains was revealed more clearly. For samples processed at 1200 °C, evidence for lamellar domains within the α_2-phase were clearly seen (Fig. 10a). However, when the sintering temperature was increased to 1300 °C, an apparent hexagonal structure developed inside the grains (Fig. 10b), confirming the hexagonal DO_{19} structure of the α_2-Ti_3Al phase [29]; this also indicated that the sintering process entered the final stage, while the grains transformed to their equilibrium shape (i.e. minimising interfacial free energy) [30].

These transformations occurred not only within the α_2 grains but also in the lamellar structure. In contrast to the small lamellar domains presented in Fig. 7 (i.e. area C), an apparent coarse lamellar structure had developed along the Ti diffusion direction, away from the cores. Figure 11 illustrates the early progress (i.e. 1200 °C) of this transformation; the lamellar expansion can be clearly seen. When the sintering temperature was increased to 1300 °C, diffusion is expected to be much faster, and consequently the coarse lamellar structure was more significantly evolved. Furthermore, under these processing conditions, the material was relatively dense, such that the aforementioned lamellar expansion area and the 'roughened' two-phase area, discussed earlier, underwent a rapid transformation due to the general absence of hindering obstacles (i.e. pores).

The progression of such massive lamellar formation, during transitioning from 1200 to 1300 °C, is highlighted in Fig. 12. As presented in Fig. 12b, after cooling the 'roughened' regions are transformed to an obviously lamellar structure, and both the grains and lamellar structures are coarsened. Larger γ-TiAl-phase regions also develop at this stage. The samples sintered at 1300 °C also presented a more homogeneous chemical composition between the grain and the lamellar structure, and both responded to the etchant with a relatively similar resistance. The grains were consequently not as noticeable as they were before the rapid transformation (i.e. when using a sintering temperature below 1300 °C). In addition, the phase evolution in the 'rough' two-phase area was more difficult to examine, because there were several morphological features presented within these regions, as highlighted in Fig. 13. The various morphologies were due to both differences in crystalline orientations and the α_2:γ ratios within the grains, each of which leads to particular responses to the etchant. The resultant microstructure resembles a more apparent 'duplex' structure, which is composed of the rounded γ grains and the α_2/γ lamellar structure (Fig. 13b).

The effects of sintering temperature, time and initial particle size are discussed in this section. Figure 14 summarises the lamellar transformation using a single α_2-Ti_3Al grain model. Such a simple configuration is adopted from the initial powder structure that contains a Ti-concentrated core. At the lower processing temperatures (i.e. <1300 °C), grain growth was contributed directly from the α_2-phase nucleation or, in most cases, from the α_2/γ-lamellar-structural formation when Ti diffuses out of the core. This newly grown area consisted of very fine lamellar structures, and could potentially be easily overlooked in the absence of suitably controlled etching. Many α_2 grains were composed of multiple subgrains, and a fine lamellar structure was also growing within some of the subgrains (Fig. 10a). At lower sintering temperatures, the lamellar structure was restricted to the fine laths, even with a longer sintering time, owing to the relatively slow diffusion kinetics. However, when the sintering temperature was increased to 1300 °C, a coarse lamellar structure emerged out of the grains, and the laths were wider and more pronounced, due to the increased thermal energy.

The phase-transformation behaviour of the composite α_2/γ regions was more complicated. The two-phase area exhibited several morphological features within the grains, as individual grains composed of various α_2:γ ratios, as well as different crystalline

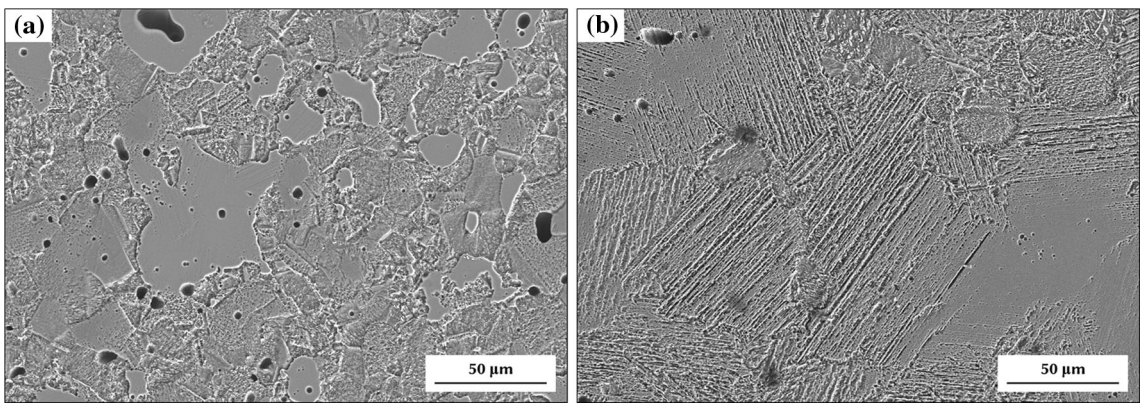

Figure 12 Representative SEM microstructural changes observed during the transitioning of SPS-processing temperatures from **a** 1200 °C/3 min to **b** 1300 °C/3 min. Both examples show combined SE/BSE images.

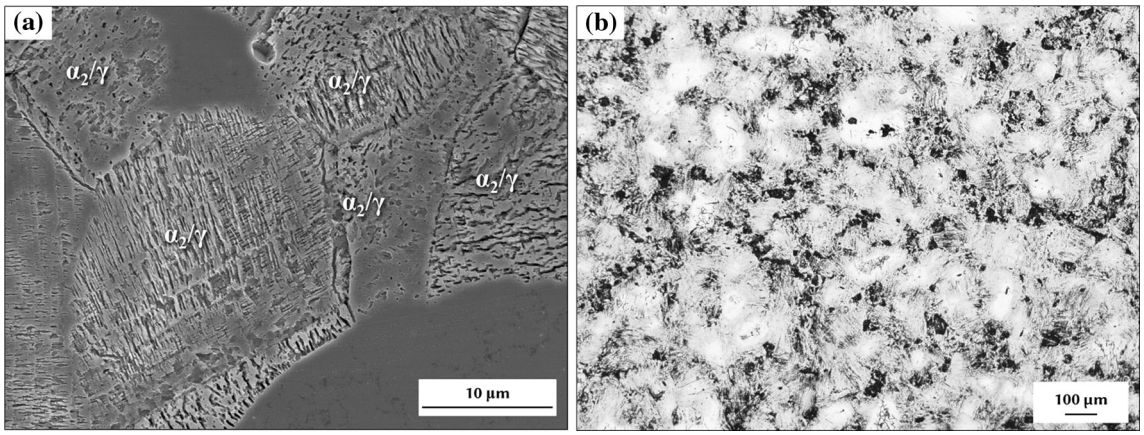

Figure 13 **a** Typical SEM image highlighting identification of the various morphological features in the two-phase area after sintering at 1200 °C/10 min (combined SE/BSE image). **b** Optical micrograph of an etched sample (SPS processed at 1300 °C/3 min), showing a 'duplex'-type structure.

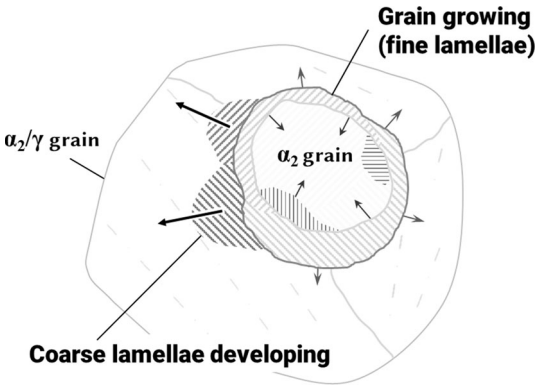

Figure 14 Proposed microstructural transformation mechanism within an α_2-Ti_3Al grain after being cooled to room temperature.

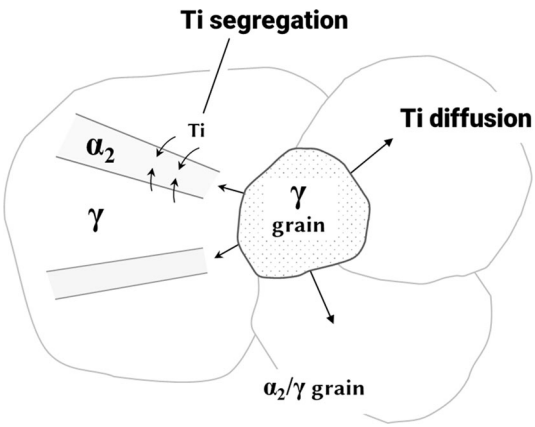

Figure 15 Schematic representation of Ti diffusion and segregation in the two-phase (α_2/γ) regions.

orientations. It is proposed that the Ti atoms segregate to the α_2-Ti_3Al phase in order to form alternating α_2- and γ-phases. Some grains which contain lower Ti initially would generally transform to a rounded γ-phase morphology, if no α_2-phase nucleates (Fig. 15). In addition, the microstructural evolution of Ti-48Al also involves the interaction of residual pores with each phase. The role of these remaining pores will be discussed in the following section.

Pore evolution and agglomeration

Pore configurations in a material can be used as an indicator in terms of the sintering stages. As densification progresses, pores shrink and their concentration invariably decreases simultaneously. However, when the densification rates gradually decrease in the final sintering stage, the pores coalesce to reduce the system (surface) energy in the material. The pores therefore undergo an Ostwald ripening stage, which describes how the larger pores grow in size at the expense of the smaller ones. In the present study, the pore size (Feret length) and associated area fraction (used as the 'pore quantity') were measured from the unetched optical micrographs, and then plotted to illustrate the pore evolution for the sintering temperature (Fig. 16a) and time (Fig. 16b), as well as the initial powder particle size (Fig. 17).

From the pore configurations evolving with temperature or time, shown in Fig. 16, both variables revealed the general trends of the Ostwald ripening stage. This phenomenon was especially obvious when examining the time effects (Fig. 16b). Initially the pore size and the area percentage both decreased

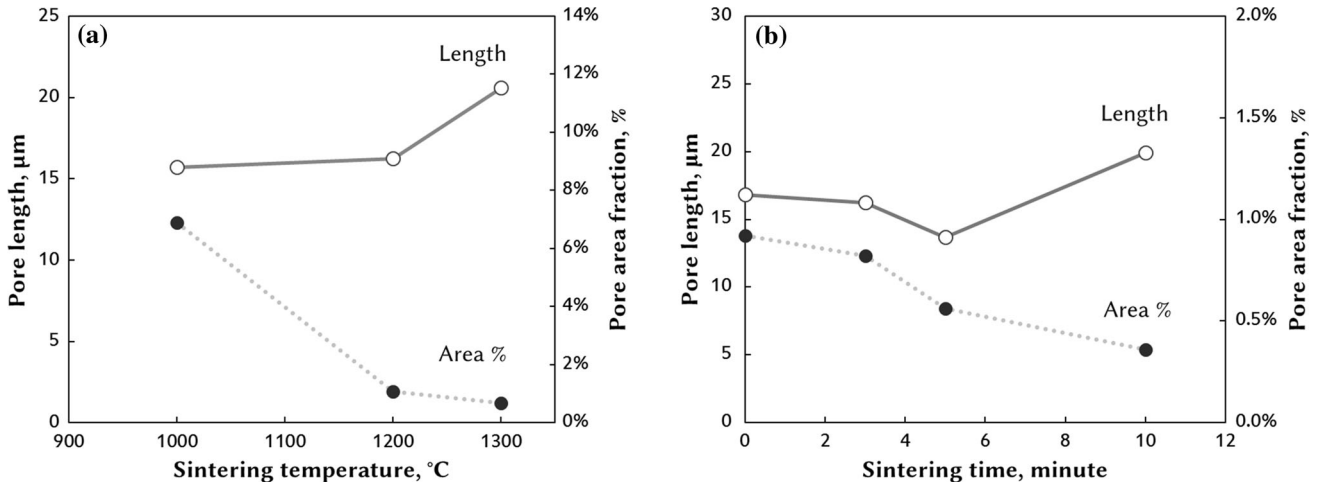

Figure 16 The pore lengths and area fractions of SPS-processed samples, showing the effects of **a** sintering temperature (held for 3 min), and **b** holding time (at a temperature of 1200 °C). Both experiments used a starting powder with $D_{50} = 56.7$ µm.

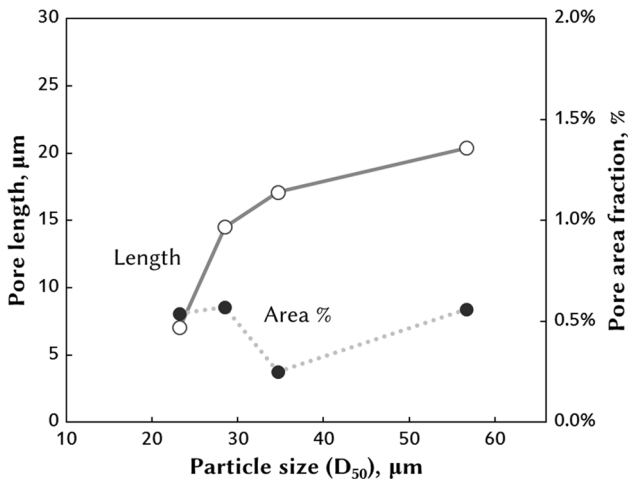

Figure 17 Starting particle size's effects on the final SPS-processing pore configuration (samples sintered at 1200 °C for 3 min).

with time, indicating densification in the material. However, when the sintering time exceeded 5 min, the pores grew noticeably, while the area percentage continued to decrease, suggesting the process had reached the final sintering stage. Further sintering would not significantly improve densification but may cause adverse pore swelling (i.e. over-sintering). Conversely, in terms of "non-thermal" parameters, specifically the starting particle size (Fig. 17), for a lower powder size the pore length decreased accordingly due to smaller voids between particles in the green compacts. The pore area fraction did not show a definite trend, in spite of the density increasing (shown in Fig. 6). It should be noted that as the porosity area fraction decreases to less than a half percent, and imaging artefacts may affect the software in determining the actual porosity content.

Furthermore, the pore locations and their associated migration were also noted under various sintering conditions. For example, in the sample sintered at 1200 °C for 5 min, larger pores were generally situated within the α_2-Ti_3Al grains (shown in lighter contrast in Fig. 18a), whereas the small pores were primarily dispersed in the two-phase region (shown in darker contrast in Fig. 18a). With a longer sintering times, the smaller pores gradually disappeared through densification, but they also coalesced to form larger pores. This observation not only confirmed the previously mentioned Ostwald ripening phenomenon, but also highlighted how the two-phase region might 'grow' (i.e. diffuse) more to eliminate the pores, while the α_2 grains grew more slowly or later in the process. As a consequence, comparatively larger pores remained in the α_2 grains. This is further supported by the previous discussions, as it is apparent that the grain (α_2) phase was developed later, after processing at a higher sintering temperature (or longer time), as evidenced by the XRD. Furthermore, the grains gradually grew around or potentially even encompassed the pores, as demonstrated in Fig. 18b. Once the pores were included within the grains, they began to aggregate. Figure 18c illustrates that the smaller pores diffused along the grain boundaries and eventually merged with the larger one in the polycrystalline particle core. Such behaviour might also occur in the lamellar phases, as

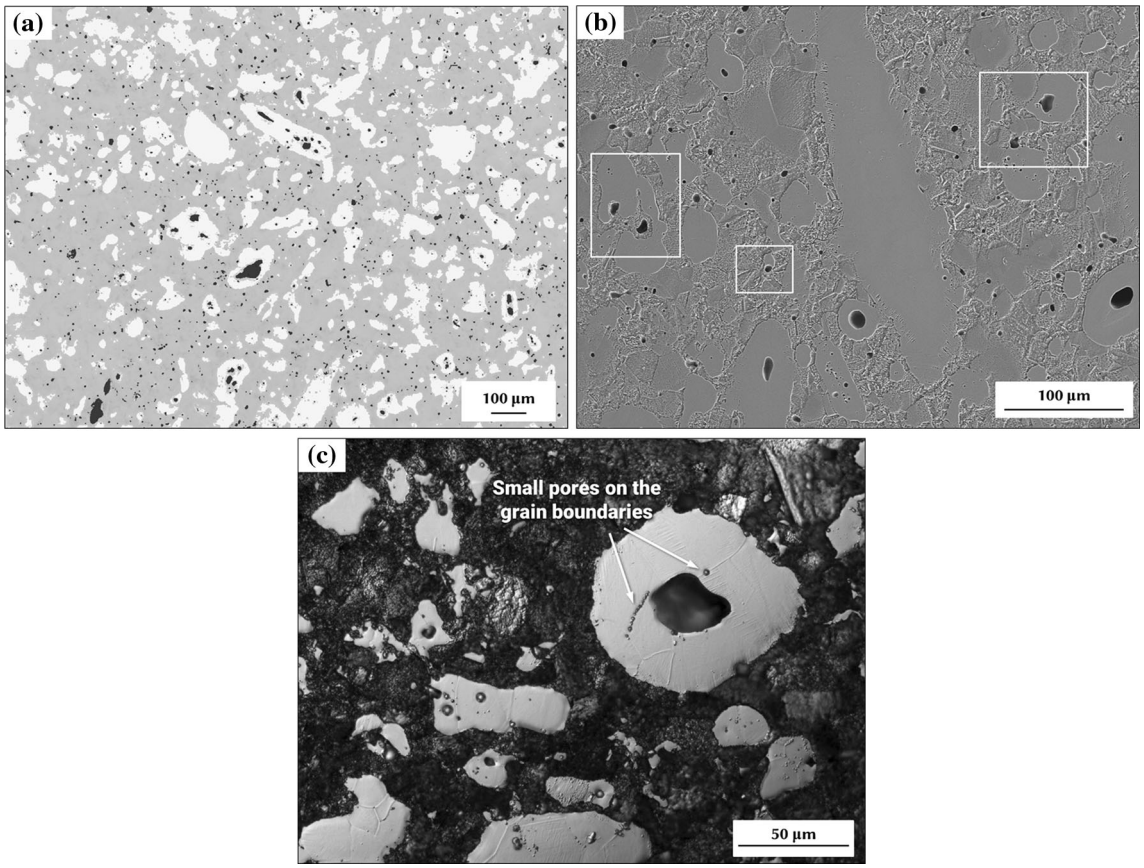

Figure 18 **a** Contrast-enhanced optical micrograph of pore locations within the sintered microstructure (1200 °C/5 min). **b** SEM micrograph showing pore entrapment after sintering at 1200 °C/3 min (combined SE/BSE image). **c** Optical micrograph of pore agglomeration (1200 °C/5 min).

there was also pore growth, although it was difficult to observe the phenomenon from the micrographs.

Conclusions

In the present study, the SPS process had shown significantly greater sintering efficiency, in terms of densification, than conventional vacuum sintering. Nearly fully dense (~98 %) Ti-48Al samples were achieved when sintering at 1200 °C with a hold time of merely 3 min. It was found that sintering longer than 3 min did not improve the densification significantly, but reduced the hardness due to grain growth. The use of a smaller starting particle size generally contributed to a finer microstructure (i.e. residual pores and grains) and slightly improved the sintered density.

During sintering, the Ti-concentrated α_2 grains could grow directly following α_2-phase nucleation, or more likely from the fine lamellar structures, which developed at lower sintering temperatures (<1200 °C). However, with the increased diffusion kinetics at higher temperatures (>1200 °C), a clear hexagonal structure developed within the grains, while the 'roughened' (i.e. α_2/γ lamellar composite structure, after etching) phase underwent a massive transformation. Coarse and long lamellar structures initiated from the edges of the grains and developed over the whole material.

As the densification progressed, the pores generally evolved following the Ostwald ripening mechanism, exhibiting a decrease in pore quantity, but an increase in mean size. The relationships between the pores and aluminide phases suggested that the 'roughened' composite areas grew faster, or earlier, as the pores were smaller and present in larger numbers in those regions. In comparison, it was shown that the α_2-Ti_3Al grains developed more slowly, or later in the process, because the pores were

larger in size and difficult to collapse, leading to the fact that the grains gradually grew around the pores.

Acknowledgements

The authors would like to gratefully acknowledge the technical support from Randy Cook and Greg Sweet. The financial support for this research comes from the Automotive Partnerships Canada (APC) programme (Grant No. APCPJ 411917-10), funded by the Natural Science and Engineering Research Council of Canada (NSERC). The authors would also like to thank Wescast Industries Inc. and Kingston Process Metallurgy Inc. for their financial, in-kind and technical supports. The supports of the Canada Foundation for Innovation, the Atlantic Innovation Fund, and other partners who helped in funding the Facilities for Materials Characterisation, managed by the Dalhousie University Institute for Materials Research, are also gratefully acknowledged.

References

[1] Takasugi T (2008) Titanium aluminide-based ntermetallic alloys. Automot Eng Light Funct Nov Mater 197

[2] Noda T (1998) Application of cast gamma TiAl for automobiles. Intermetallics 6:709–713. doi:10.1016/S0966-9795(98)00060-0

[3] Lagos MA, Agote I (2013) SPS synthesis and consolidation of TiAl alloys from elemental powders: microstructure evolution. Intermetallics 36:51–56. doi:10.1016/j.intermet.2013.01.006

[4] Bartolotta P, Barrett J, Kelly T, Smashey R (1997) The use of cast Ti-48Al-2Cr-2Nb in jet engines. JOM 49:48–50. doi:10.1007/BF02914685

[5] Wang YH, Lin JP, He YH et al (2006) Reaction mechanism in high Nb containing TiAl alloy by elemental powder metallurgy. Trans Nonferrous Met Soc China Engl Ed 16:853–857. doi:10.1016/S1003-6326(06)60339-7

[6] Schloffer M, Iqbal F, Gabrisch H et al (2012) Microstructure development and hardness of a powder metallurgical multi phase γ-TiAl based alloy. Intermetallics 22:231–240. doi:10.1016/j.intermet.2011.11.015

[7] Lee T, Kim J, Hwang S (1997) Direct consolidation of γ-TiAl-Mn-Mo from elemental powder mixtures and control of porosity through a basic study of powder reactions. Metall Mater Trans A 28:2723

[8] Wang YH, Lin JP, He YH et al (2009) Microstructural characteristics of Ti-45Al-8.5Nb/TiB2 composites by powder metallurgy. J Alloys Compd 468:505–511. doi:10.1016/j.jallcom.2008.01.057

[9] Liu K, Ma YC, Gao M et al (2005) Single step centrifugal casting TiAl automotive valves. Intermetallics 13:925–928. doi:10.1016/j.intermet.2004.12.004

[10] Jovanović MTT, Dimčić B, Bobić I et al (2005) Microstructure and mechanical properties of precision cast TiAl turbocharger wheel. J Mater Process Technol 167:14–21. doi:10.1016/j.jmatprotec.2005.03.019

[11] Chandley D (2000) Use of gamma titanium aluminide for automotive engine valves. Metall Sci Technol 18(1):8–11

[12] Daloz D, Hecht U, Zollinger J et al (2011) Microsegregation, macrosegregation and related phase transformations in TiAl alloys. Intermetallics 19:749–756. doi:10.1016/j.intermet.2010.11.013

[13] Xiao S, Tian J, Xu L et al (2009) Microstructures and mechanical properties of TiAl alloy prepared by spark plasma sintering. Trans Nonferrous Met Soc China 19:1423–1427. doi:10.1016/S1003-6326(09)60044-3

[14] Couret A, Molénat G, Galy J, Thomas M (2008) Microstructures and mechanical properties of TiAl alloys consolidated by spark plasma sintering. Intermetallics 16:1134–1141. doi:10.1016/j.intermet.2008.06.015

[15] Guyon J, Hazotte A, Monchoux JP, Bouzy E (2013) Effect of powder state on spark plasma sintering of TiAl alloys. Intermetallics 34:94–100. doi:10.1016/j.intermet.2012.11.005

[16] Jabbar H, Monchoux J-P, Thomas M, Couret A (2011) Microstructures and deformation mechanisms of a G4 TiAl alloy produced by spark plasma sintering. Acta Mater 59:7574–7585. doi:10.1016/j.actamat.2011.09.001

[17] Suárez M, Fernández A, Menéndez J (2013) Challenges and opportunities for spark plasma sintering: a key technology for a new generation of materials. Sinter Appl. doi:10.5772/53706

[18] Saheb N, Iqbal Z, Khalil A et al (2012) Spark plasma sintering of metals and metal matrix nanocomposites: a review. J Nanomater. doi:10.1155/2012/983470

[19] Calderon HA, Garibay-febles V, Umemoto M, Yamaguchi M (2002) Mechanical properties of nanocrystalline Ti-Al-X alloys. Mater Sci Eng A 331:196–205

[20] Liu Y, Huang BY, He YH, Zhou KC (2000) Processing TiAl-based alloy by elemental powder metallurgy. J Mater Sci Technol 16:605–610

[21] Munir ZA, Anselmi-Tamburini U, Ohyanagi M (2006) The effect of electric field and pressure on the synthesis and consolidation of materials: a review of the spark plasma sintering method. J Mater Sci 41:763–777. doi:10.1007/s10853-006-6555-2

[22] Kulkarni KN, Sun Y, Sachdev AK, Lavernia E (2013) Field-activated sintering of blended elemental γ-TiAl powder

compacts: porosity analysis and growth kinetics of Al3Ti. Scr Mater 68:841–844. doi:10.1016/j.scriptamat.2013.02.004

[23] Sun ZM, Wang Q, Hashimoto H et al (2003) Synthesis and consolidation of TiAl by MA-PDS process from sponge-Ti and chip-Al. Intermetallics 11:63–69. doi:10.1016/S0966-9795(02)00183-8

[24] Rawers JC, Wrzesinski WR (1992) Reaction-sintered hot-pressed TiAl. J Mater Sci 27:2877–2886. doi:10.1007/BF01154095

[25] Chen YY, Yu HB, Zhang DL, Chai LH (2009) Effect of spark plasma sintering temperature on microstructure and mechanical properties of an ultrafine grained TiAl intermetallic alloy. Mater Sci Eng A 525:166–173. doi:10.1016/j.msea.2009.06.056

[26] Weston NS, Derguti F, Tudball A, Jackson M (2015) Spark plasma sintering of commercial and development titanium alloy powders. J Mater Sci 50:4860–4878. doi:10.1007/s10853-015-9029-6

[27] Wen CE, Yasue K, Yamada Y (2001) Fabrication of TiAl by blended elemental powder semisolid forming. J Mater Sci 36:1741–1745. doi:10.1023/A:1017572624976

[28] Kainuma R, Palm M, Inden G (1994) Solid-phase equilibria in the Ti-rich part of the Ti-Al system. Intermetallics 2:321–332. doi:10.1016/0966-9795(94)90018-3

[29] Kim YWY (1994) Ordered intermetallic alloys, part III: gamma titanium aluminides. JOM 46:30–39. doi:10.1007/BF03220745

[30] Porter DA, Easterling KE, Sherif M (2009) Phase transformations in metals and alloys, 3rd edn (revised reprint). CRC Press, Boca Raton